

GRID-WORLD REPRESENTATIONS IN TRANSFORMERS REFLECT PREDICTIVE GEOMETRY

Sasha Brenner

Max Planck Institute for Human Cognitive and Brain Sciences, Leipzig, Germany
Leipzig University, Germany
brenner@cbs.mpg.de

Thomas R. Knösche*

Max Planck Institute for Human Cognitive and Brain Sciences, Leipzig, Germany
knoesche@cbs.mpg.de

Nico Scherf*

Max Planck Institute for Human Cognitive and Brain Sciences, Leipzig, Germany
Center for Scalable Data Analytics and Artificial Intelligence (ScaDS.AI), Dresden/Leipzig, Germany
nscherf@cbs.mpg.de

ABSTRACT

Next-token predictors often appear to develop internal representations of the latent world and its rules. The probabilistic nature of these models suggests a deep connection between the structure of the world and the geometry of probability distributions. In order to understand this link more precisely, we use a minimal stochastic process as a controlled setting: constrained random walks on a two-dimensional lattice that must reach a fixed endpoint after a predetermined number of steps. Optimal prediction of this process solely depends on a sufficient vector determined by the walker’s position relative to the target and the remaining time horizon; in other words, the probability distributions are parametrized by the world’s geometry. We train decoder-only transformers on prefixes sampled from the exact distribution of these walks and compare their hidden activations to the analytically derived sufficient vectors. Across models and layers, the learned representations align strongly with the ground-truth predictive vectors and are often low-dimensional. This provides a concrete example in which world-model-like representations can be directly traced back to the predictive geometry of the data itself. Although demonstrated in a simplified toy system, the analysis suggests that geometric representations supporting optimal prediction may provide a useful lens for studying how neural networks internalize grammatical and other structural constraints.

1 INTRODUCTION

Large language models (LLMs) have proven to be extremely powerful and scalable models, but they are trained on a famously simple objective function: probability estimation of the next token in a sequence (Radford et al. (2019); Brown et al. (2020)). While being fundamentally probabilistic, these models must simultaneously learn strict syntax and subtle semantics, and their ability to do this scales with the number of parameters and the amount of training data (Kaplan et al. (2020)). This leads to the question of how natural grammar is internally encoded in the models, and whether

*These authors contributed equally.

these representations can even be interpreted. Indeed, plenty of research has tried to answer these questions since the early days of transformer-based LLMs, providing interesting insights (López-Otal et al. (2025); Ferrando et al. (2024); Rogers et al. (2021)). Notably, much of this prior work indicates that very similar grammar-like representations often emerge during learning for different models (Manning et al. (2020); Diego-Simón et al. (2024); Liu et al. (2019)), which suggests that such structures may be implicit in the data distribution and that learning them could facilitate optimization.

While it seems obvious that grammatical rules are implicit in any language dataset, placing that statement on solid theoretical grounds could be more challenging. A quantitative framework of natural grammar is desirable in the study of neural network interpretability, because it could provide formal objects amenable to existing techniques, including those from representational analysis (Sucholutsky et al. (2023)). Since frontier LLMs are based on neural network architectures trained on information-theoretic objectives, a reasonable theoretical foundation should be able to describe grammatical structures in terms of probability distributions and feature spaces. The foundations for such a framework indeed exist; a long tradition in natural language processing (NLP) and computational linguistics focuses on the distributional aspects of linguistic elements (Sahlgren (2008); Boleda (2020); Turney and Pantel (2010)), and it laid part of the conceptual groundwork for the Transformer architecture behind most frontier LLMs (Vaswani et al. (2017)).

Related to the question of how neural networks represent grammar is the concept of world models. Auto-regressive foundation models have been shown to encode geometric information about the semantic content of the token sequences being parsed; in other words, they seem to model the world their inputs refer to (Gurnee and Tegmark (2024); Karvonen (2024); Ivanitskiy et al. (2023)). This is consistent with proposals attributing LLMs’ success in in-context learning to latent-structure inference (Xie et al. (2022)), echoing the idea of world models in the field of reinforcement learning, where agents can benefit from compressed representations of the complex environments they interact with (Ha and Schmidhuber (2018); Hafner et al. (2025); Hansen et al. (2024)). The presumed reason is that only a small set of latent variables in these environments are actually relevant for optimal prediction and control, and identifying them greatly reduces costs. This hints at the close relationship between world modeling and prediction, which is the basic language-modeling objective.

Here, we use a deliberately minimal toy setting to explore how grammar-like constraints can be represented in sequence models through the lens of optimal prediction and computational mechanics, following a recent line of interpretability research (Shai et al. (2024); Piotrowski et al. (2025); Riechers et al. (2025b); Shai et al. (2026)). This framework infers the computational properties of stochastic processes by keeping track of their *causal states*, sets of observation sequences which are exclusively defined by their predictions of the future (Crutchfield and Young (1989); Shalizi and Crutchfield (2001)). Every stochastic process is therefore uniquely characterized by the topology and geometry of its causal-state network. Since LLMs are models of stochastic processes, linguistic structure may be reflected in topological and geometric regularities of the data distribution. If such regularities exist, neural networks trained for next-token prediction may learn internal representations that capture them, particularly when doing so improves predictive accuracy and robustness. Although instantiating this as a concrete hypothesis for natural language is an ambitious goal, we may study smaller toy settings as a start to collect insights, a strategy that has already shown to be fruitful in this context (Piotrowski et al. (2025)). We therefore focus on a set of toy regular grammars generated by the movements of a random walker on a square lattice with a single constraint: it must, after a fixed number of time steps, arrive at some predetermined location on the grid. While vastly simpler than a full-fledged natural language, this grid walker has the advantage of providing a highly interpretable ground truth with analytic solutions, which we believe is key at this stage. Additionally, the random generation of sequences in these grammars is a non-stationary and non-ergodic process, like real language generation is. This is a relevant generalization with respect to prior systems studied under this framework.

We computed the exact joint probability distributions of sequences for a few grid walkers, each with its own characteristic length and endpoint. Decoder-only transformers were then trained on

samples taken from the exact marginal distributions of prefix sequences. We consistently found low-dimensional representations that closely align with probability vectors of prediction, similarly to what was reported in Shai et al. (2024) for other types of hidden-Markov models (HMMs). These representations emerged in most internal layers of the trained transformers, but their geometries slightly varied across different layers and layer types. While such representations are extracted in a principled way from predictive distributions, they suggestively resemble a grid-world model. Our simple toy model thus illustrates a concrete mechanism through which grammar and world models can directly emerge from the geometry of probability distributions. While this observation does not establish that the same mechanism applies to natural language, it provides a tractable example in which the relationship can be analyzed exactly.

The remainder of this paper is organized as follows. Section 2 reviews prior work on predictive and belief-state representations, grammatical structure in language models, and emergent world models. Section 3 introduces the constrained grid-walker process and presents the analytical quantities used for training and evaluation. Section 4 reports representational-alignment results across layers and model configurations, along with their interpretation in terms of predictive geometry. Section 5 discusses limitations and open challenges, and Section 6 concludes.

2 RELATED WORK

2.1 BELIEF-STATE REPRESENTATIONS IN NEURAL NETWORKS

We largely base ourselves on a novel line of work that places large-language-model (LLM) interpretability under the lens of optimal prediction (Shai et al. (2024); Piotrowski et al. (2025); Riechers et al. (2025b); Riechers et al. (2025a)). Specifically relevant to it is a theoretical framework known as *computational mechanics*, which studies dynamical and stochastic systems by identifying the minimal information about the past needed for optimal prediction of the future. In particular, when the latent generative mechanism is a homogeneous hidden Markov model (HMM), this minimally sufficient predictive information coincides with the *belief state*, *i.e.*, the probability distribution over the hidden states of the HMM.

In Shai et al. (2024), the authors trained transformers on sequences generated by a set of small but highly unpredictable edge-emitting HMMs. They found parsimonious linear mappings from the layer representations to the HMM’s belief states within the hidden-state simplex. The authors’ explanation is that belief-state representations might allow models to perform belief updates at each successive timestep of the input sequences. Indeed, a concrete mechanistic implementation of belief updating was proposed in the context of self-attention in a later paper (Piotrowski et al. (2025)), and evidence for it was provided. Evidence for representational alignment with belief states has also been reported for different variants of RNN architectures (Riechers et al. (2025b)).

Furthermore, a more general set of latent generative models was tested in Riechers et al. (2025b): generalized hidden Markov models (GHMMs). These include HMMs, but also other non-Markovian systems that nevertheless still enjoy a Markov-style update rule over some set of generalized belief states, which do not necessarily correspond to probability distributions over states (but are related to them).

In all studied examples, however, the processes were stationary and ergodic. Since we are interested in formal and natural languages, which are generally neither ergodic nor stationary, studying predictive-state representations on such systems in a simple case like our grid walker is an important first step in this direction. Moreover, most belief states analyzed by the authors were restricted to a flat manifold (although it often featured fractal structure within). In contrast, the grid walker’s predictive states are contained in a curved manifold within the probability simplex. There is, in addition, a formal distinction to be made between predictive and belief states, which is briefly discussed in Section 4.4.

2.2 GRAMMAR AND STRUCTURE IN LARGE LANGUAGE MODELS

There is extensive work analyzing how grammatical structure is reflected in neural language models trained on natural text (Manning et al. (2020); López-Otal et al. (2025)). A common approach is to test whether syntactic information is recoverable from internal activations, using probing-style methods and geometric diagnostics (Peters et al. (2018); Liu et al. (2019); Tenney et al. (2019); Hewitt and Manning (2019); Wu et al. (2020); Coenen et al. (2019); Diego-Simón et al. (2024)). Other work inspects model components more directly by studying attention patterns and head specialization (Clark et al. (2019); Htut et al. (2019); Vig and Belinkov (2019); Voita et al. (2019)). To move beyond correlational evidence, interventionist and causal analyses attempt to test whether hypothesized syntactic variables are actually used, and to localize intermediate computations (Tucker et al. (2021); Finlayson et al. (2021); Lepori et al. (2024)).

While this literature provides many useful techniques, the combination of massive models and the complexity of natural language makes it difficult to isolate mechanisms cleanly. Our goal is therefore not to compete on linguistic coverage, but to study a small but controlled setting where the relevant predictive structure is explicit, allowing a sharp test of the link between optimal prediction, representation geometry, and grammatical constraints.

2.3 EMERGENT WORLD MODELS

Recent literature asks whether next-token predictors learn internal representations that function as *world models*. Early evidence in a controlled setting came from a GPT model trained on Othello move sequences, which developed an emergent internal representation of the board state that could be used to control model outputs via interventions (Li et al. (2023)). Similar findings were subsequently reported for chess-playing language models (Karvonen (2024)). In large-scale LLMs, representations have been shown to encode linear structure for space and time (Gurnee and Tegmark (2024)). Complementary evidence comes from maze-solving tasks, where transformers develop structured internal representations of topology and paths (Ivanitskiy et al. (2023)). Across all these settings, however, establishing *why* the next-token prediction objective should give rise to world-model geometry has proven elusive: the complexity of the tasks makes it difficult to trace learned representations back analytically to the statistical structure of the data.

3 METHODS

We work in a setting where the ground truth is available exactly: constrained random walkers on a 2-dimensional square lattice; *walkers* for short. For each walker configuration, we compute the full next-step probability distribution analytically, train decoder-only transformers from scratch on prefix sequence samples drawn from these distributions with a next-token cross-entropy loss, and then evaluate learned hidden states by fitting linear probes to the analytically derived sufficient predictive vectors across layers. Most of the code and hyperparameter choices are based on the public repository used in Riechers et al. (2025b). Below is a detailed explanation of the methods.

3.1 THE GRID WALKER

We use the grid walker as a deliberately minimal toy model to assess whether and how simple grammatical rules can be recovered from the internal representations of neural networks and interpreted as vectors for optimal prediction. In this subsection, we show how the walker’s predictive structure can be derived analytically and summarized by low-dimensional sufficient statistics.

Grid walkers are stochastic systems that move on an infinite 2D square lattice isomorphic to \mathbb{Z}^2 . At each discrete timestep t , the walker can move either left (L), right (R), down (D), or up (U). Each of these actions corresponds to a displacement vector in the set

$$\mathcal{E} = \{\Delta_L, \Delta_R, \Delta_D, \Delta_U\}, \tag{1}$$

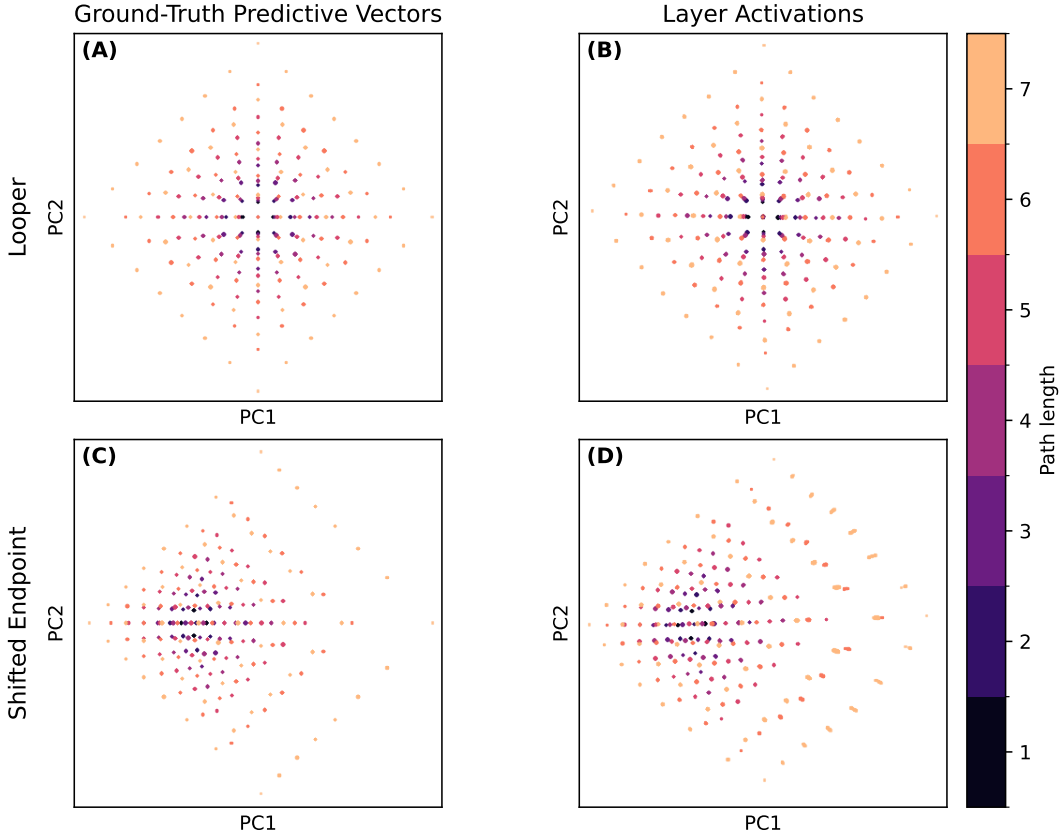


Figure 1: Transformer layer representations closely resemble the ground-truth predictive vectors of Equation 4 (as computed in Appendix A.3). The left column corresponds to the ground-truth principal components (PCs), and the right column shows the PCs of the last layer norm representation, after Procrustes-alignment to the ground-truth vectors. Each point represents a distinct sequence of movements on the square lattice, colored by the number of steps (path length). These representations could be interpreted as grid-world models, and they simply correspond to minimal and sufficient vectors for prediction.

where $\Delta_L = (-1, 0)$, $\Delta_R = (1, 0)$, $\Delta_D = (0, -1)$, and $\Delta_U = (0, 1)$.

More specifically, we study walkers with a single constraint: they must reach some endpoint \mathbf{p} after a fixed number of timesteps T . Thus, each walker is uniquely and fully characterized by the number T and the position vector \mathbf{p} ; we refer to paths of length T that reach \mathbf{p} as *valid paths*.

The finite set of all valid paths constitutes a regular language with vocabulary $\{L, R, D, U\}$. Its rules can be algebraically expressed in a simple way: keep a position vector $\mathbf{x}_t := \mathbf{x}(s_t) = (x, y)$ associated to s_t and perform the update

$$\mathbf{x}_{t+1} = \mathbf{x}_t + \Delta_t$$

at each timestep t , where $c_t \in \{L, R, D, U\}$ and $\Delta_t := \Delta(c_t) \in \mathcal{E}$ is a displacement vector from Equation 1; the string $s_T \in \{L, R, D, U\}^T$ is then accepted if and only if $\mathbf{x}_T = \mathbf{p}$. Note that $\mathbf{x}_t = \sum_{t'=1}^t \Delta_{t'}$.

In order to make these systems stochastic, we define the symbol random variables C_t and the strings $S_t = \sum_{t'=1}^t C_{t'} \in \{L, R, D, U\}^t$, where the sum of symbols or strings indicates concatenation. Furthermore, we only consider walkers for which, given the endpoint, all paths of length T leading to it are equally likely. Symbolically, $S_T \sim \text{Unif}\{s_T : \mathbf{x}(s_T) = \mathbf{p}\}$. Partial walks of length $t < T$,

by contrast, are not uniformly distributed: their probability is proportional to the number of valid completions of the prefix, a quantity formally defined and approximated in Appendix A.1.

The expression for the next-step probability is particularly relevant considering the predictive nature of the neural network models under scrutiny (see Appendix A.2 for its derivation),

$$\Pr(c_{t+1}|s_t; \mathbf{p}) \approx \frac{e^{-\mathbf{v}_t \cdot \Delta_{t+1}}}{\sum_{\Delta'_{t+1} \in \mathcal{E}} e^{-\mathbf{v}_t \cdot \Delta'_{t+1}}}, \quad (2)$$

$$\mathbf{v}_t := \mathbf{q} \left(\frac{\mathbf{x}_t - \mathbf{p}}{T - t - 1} \right), \quad (3)$$

where \mathbf{q} is a non-linear, real-analytic vector function (see Appendix A.3). Equation 2 is the Softmax function applied to the logit vector $-D\mathbf{v}_t$, where D is a 4×2 matrix with the elements of \mathcal{E} as columns. This expression is valid for $t \ll T$. Analyticity of \mathbf{q} entails that the logit vectors $-D\mathbf{v}_t$ lie on some curved 2-dimensional manifold. In the *diffusive regime* $\|\mathbf{x}_t - \mathbf{p}\| \ll T - t$, \mathbf{q} can be linearized and yields

$$\Pr(c_{t+1}|s_t; \mathbf{p}) \Big|_{\text{diffusive}} \approx \frac{e^{-2 \frac{\mathbf{x}_t - \mathbf{p}}{T - t - 1} \cdot \Delta_{t+1}}}{\sum_{\Delta'_{t+1} \in \mathcal{E}} e^{-2 \frac{\mathbf{x}_t - \mathbf{p}}{T - t - 1} \cdot \Delta'_{t+1}}}, \quad (4)$$

where the logit vectors now lie on a plane.

Equation 2 tells us that knowledge of \mathbf{v}_t , a single 2D state vector given by Equation 3, is sufficient to make any future predictions of the system. For this reason, we refer to \mathbf{v}_t as the *sufficient vector*. In practice, we compute it by inverting Equation 2, as explained in Appendix A.3. In Section 4, we show evidence that Transformers tend to autonomously find this representation during training.

3.2 DATA GENERATION

In practice, the neural networks that we use never sample full length- T sequences; rather, we train the models on length- τ prefixes (with fixed $\tau = 8$) drawn from the marginal distribution over prefixes induced by the full conditioned process (Equation 5 in Appendix A.1). In order to compute the full distribution, we use a dynamic programming algorithm (more details in Appendix A.1).

We trained six identical transformer neural networks, each on one of the six distinct grid walkers listed in Table 1. Three time horizons T were chosen for walkers looping back to the origin, to test three different regimes of τ/T : a small, medium and big loop relative to the prefix length; these correspond to walkers 1, 2 and 3 in Table 1, and we will refer to them as *loopers*. Three additional walkers with shifted endpoint $\mathbf{p} = (4, 0)$ were set up for the same three values of T , corresponding to walkers 4, 5 and 6.

3.3 SAMPLING, TRAINING AND VALIDATION

Samples for training are drawn with replacement from the marginal distribution in batches. As prediction objective, we use a next-token cross-entropy loss over all positions of the input sequences averaged over the minibatch, with the first loss term corresponding to predicting s_2 given s_1 (no beginning-of-sequence token). All models are optimized using the Adam algorithm during training. We refer to Appendix A.6 for a comprehensive list of hyperparameters used.

Validation uses exact expected cross-entropy loss under the ground-truth distribution. The per-token loss is calculated as in training, but instead of the sample mean of a minibatch, we compute a weighted average over the entire set of possible prefixes at every validation round, where each partial sequence’s per-token loss is weighted by its exact ground-truth probability. Importantly, this validation paradigm does not measure generalization, but controls for the global optimization problem. Final validation losses of the trained models are shown in Table 1 with respect to a baseline theoretical loss given by the ground-truth conditional entropy of an observation given a history.

Table 1: Walkers used for training. The last column shows the mean excess validation loss with respect to the theoretical lower bound after 20 000 epochs. The loss lower bound for the n^{th} token is its conditional entropy given all previous $n - 1$ observations according to the exact probability distribution of the system. The excess loss shown in this table is an average over all sequences of length between 2 and 8, each with its own baseline units. All values are close to zero, confirming that every model has learned to predict the sequence distribution to near-theoretical-optimal accuracy.

INDEX	ENDPOINT p	HORIZON T	MEAN VAL LOSS
1	(0, 0)	20	$4.5 \cdot 10^{-6}$
2	(0, 0)	200	$2.6 \cdot 10^{-7}$
3	(0, 0)	1000	$5.5 \cdot 10^{-5}$
4	(4, 0)	20	$5.9 \cdot 10^{-6}$
5	(4, 0)	200	$< 10^{-8}$
6	(4, 0)	1000	$< 10^{-8}$

3.4 REPRESENTATIONAL ANALYSIS

We wish to evaluate the degree of alignment between the transformer layer representations and the sufficient vectors given by Equation 3. In order to do this, we rely on two separate quantities: the coefficient of determination (R^2) of a least-squares affine map between the two representations, and the linear centered kernel alignment (ICKA), a widely used representational similarity metric (Kornblith et al. (2019)).

We compute an affine map from activations to ground-truth targets. This is obtained after a weighted least-squares minimization. Explicitly, given all prefixes s_t of length $t \leq \tau$, their respective layer ℓ activations $\mathbf{a}_\ell(s_t) \in \mathbb{R}^{d_\ell}$ and mean-centered log-probability vectors $\bar{\ell}_t \in \mathbb{R}^4$ (Appendix A.3),

$$\hat{W}_\ell, \hat{\mathbf{b}}_\ell = \arg \min_{W_\ell, \mathbf{b}_\ell} \sum_{t=1}^{\tau} \sum_{s_t} \frac{1}{n(s_t, t)} \|W_\ell \mathbf{a}_\ell(s_t) + \mathbf{b}_\ell - \bar{\ell}_t\|^2,$$

where the matrix $W_\ell \in \mathbb{R}^{4 \times d_\ell}$, together with the vector $\mathbf{b}_\ell \in \mathbb{R}^4$, are the parameters of the affine transformation, and $n(s_t, t)$ designates the degeneracy of s_t , *i.e.*, the total number of length- t sequences that are equivalent to s_t in the sense that they are also characterized by the triplet (\mathbf{x}_t, t) ; we apply the weights $w(s_t) = n(s_t, t)^{-1}$ to more accurately reflect the global geometry of the representation. To obtain an unbiased measure of alignment, we evaluate using a leave-one-group-out cross-validated weighted R^2 : for each equivalence class (\mathbf{x}_t, t) , the affine map is re-fitted on all remaining classes and applied to predict the held-out class. The residuals are then pooled across all groups to yield a single R^2 estimate that reflects out-of-sample generalization.

The second similarity coefficient that we use is the ICKA. It essentially computes the linear correlation between the centered covariance matrices of both representations. Explicitly,

$$\text{ICKA} = \frac{\|A_\ell^\top L_t\|_{\text{F}}^2}{\|L_t^\top L_t\|_{\text{F}} \|A_\ell^\top A_\ell\|_{\text{F}}},$$

where A_ℓ is the matrix with the weighted-centered and scaled versions of vectors $\mathbf{a}_\ell(s_t)$ as rows, and each row represents a distinct prefix s_t ; analogously, L_t is the matrix with the weighted-centered and scaled versions of vectors $\bar{\ell}_t$ as rows. The weights used for centering and scaling are the inverse degeneracies $w(s_t)$ described above.

The main difference between these two metrics—apart from the fact that held-out test sets are used in R^2 computations—is that the R^2 coefficient ignores the neural network’s feature-space variance altogether, whereas ICKA filters out directions of low variance in feature space (Kornblith et al. (2019)).

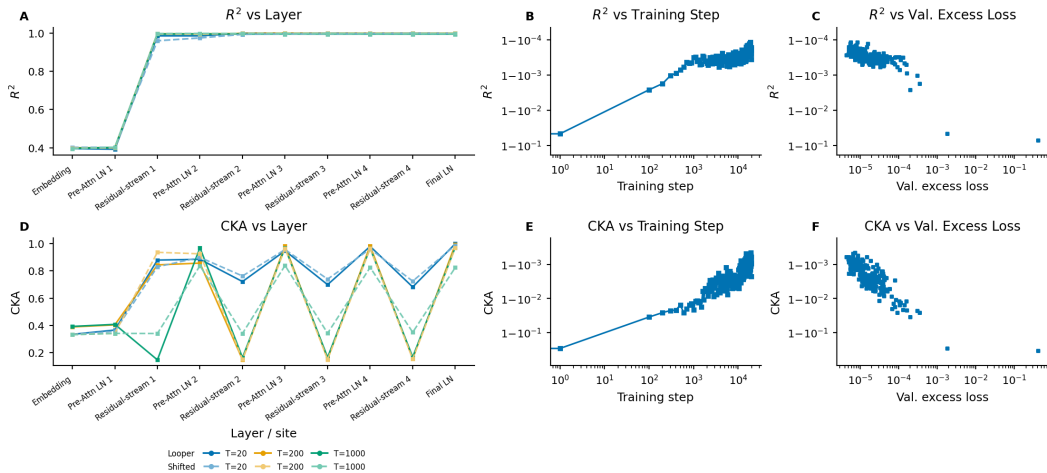


Figure 2: Linear similarity metrics between layer activations and ground-truth predictive vectors. (A) and (D): Both R^2 and lCKA are high and tend to increase with layer depth, with Layer-Norms generally exhibiting stronger similarity. Moreover, walkers with longer time horizons T have worse similarity scores given an endpoint, while loopers’ scores are higher in comparison to shifted-endpoint walkers’ ones for a given time horizon. In these plots, lines corresponding to loopers are solid, while those associated with shifted-endpoint walkers are dashed. (B-C): The R^2 value for the $T = 20$ looper is shown as a function of the training step in (B), and it is compared with the excess validation loss from its corresponding timestep in (C). (E-F) The lCKA value for the same $T = 20$ looper is also shown as a function of training step (E) and compared to the loss (F).

4 RESULTS AND DISCUSSION

We trained six identical transformers on six different grid walkers respectively, as shown in Table 1 and detailed in Section 3.2. In Section 3.1, we showed that knowledge of a 2-dimensional state vector \mathbf{v}_t (Equation 3) is sufficient to make predictions. We hypothesized that the network finds this representation of the input. Figure 1 shows the first two principal components of both the ground-truth sufficient vectors and final LayerNorm activations for walkers 1 and 4 of Table 1, where the resemblance becomes evident.

4.1 NETWORK ACTIVATIONS MATCH PREDICTIVE GEOMETRIES

We compare layer activations and ground-truth predictive vectors using two metrics: the coefficient of determination (R^2) of the linear mapping and the linear centered kernel alignment (lCKA), both described in Section 3.4. They are shown in Figure 2 for every walker and for each layer of the residual stream and pre-attention LayerNorms. The linear agreement between most layer representations and the ground-truth predictive vector \mathbf{v}_t was high. LayerNorm representations, however, showed a visibly higher lCKA with respect to the ground truth, whereas residual stream vectors had a poorer linear readability. R^2 did not vary as much as the lCKA, suggesting that the first overestimates alignment.

Although one might reasonably anticipate a strong match between pre-readout activations and the vectors \mathbf{v}_t , there was no guarantee that such alignment would also occur for the other LayerNorm representations. To be precise, final LayerNorm alignment makes sense because the transformer output logits are fitted to the ground-truth logits during training; but these two are just affine-transformed versions of, respectively, the final LayerNorm activations and the predictive vectors \mathbf{v}_t —under this light, their fit is foreseeable. In contrast, early and intermediate activations are less obviously constrained by the output layer; they are not strictly required to represent this predictive geometry linearly, but they seem to do so, at least to some extent.

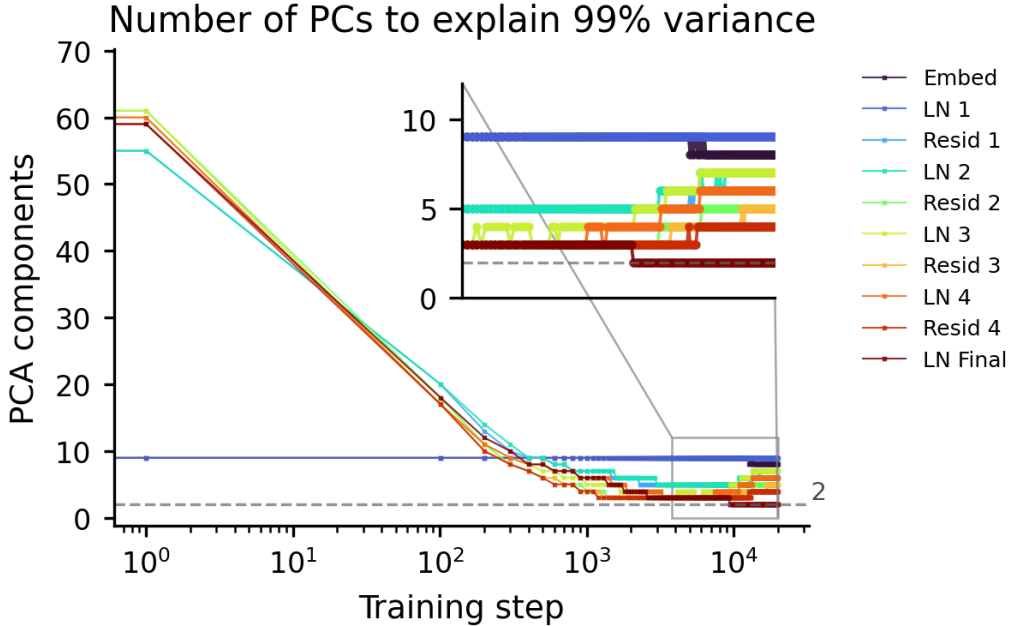


Figure 3: For the $T = 20$ looper, the number of principal components required to explain 99% of the variance converges to 2 for the final LayerNorm’s activations, but it rebounds for all previous hidden layers after around 10^4 training steps.

To analyze the intrinsic dimensionality of the representations, we perform principal component analysis (PCA) on the layer activations at each training checkpoint, treating each prefix in the dataset as a sample in the analysis. As in the computation of the alignment measures, we apply the same weights of inverse degeneracy to the samples (see Section 3.4). In Figure 3, we show the required number of principal components needed to explain 99% of the variance of each layer across training for the $T = 20$ looper. The final LayerNorm converges to a 2-dimensional representation (Figure 1B), even though the activation space as a whole is 128-dimensional. While Equation 4 does seem to suggest that logits at the final layer should be constrained to a 2-dimensional space, the Softmax function actually has a gauge freedom: any arbitrary function of \mathbf{x}_t can be added to the logits without changing the next-step distribution. In other words, the network did not strictly need to find such a flat representation. It is not rare, however, for networks to find low-dimensional representations (even nonlinear ones Ansuini et al. (2019)). Curiously, the number of dimensions spanned by the rest of the layer representations seems to converge first, but then rebounds slightly halfway through training.

4.2 PREDICTIVE GEOMETRY AS A WORLD MODEL

In Section 4.1, we argued how the alignment between the last LayerNorm activations and the predictive vectors \mathbf{v}_t defined by Equation 3 is rather unsurprising from a purely mathematical perspective. This seemingly trivial result, however, might hint at a valuable insight. One may imagine the scenario of encountering the internal representations of Figures 1B and 1D without any knowledge of the predictive geometry, *i.e.*, Figures 1A and 1C. At first glance, the emergent representations of the model would seem to replicate the known structure of the grid world that the data is generated from. Since world models can improve prediction and control in many different machine learning settings, this alone could explain away the benefits of such representations. In more complex contexts, finding such a world representation sometimes entails a result of its own. The simple grid walkers we study illustrate a way in which world models can be directly extracted from the predic-

tive structure of the system. Indeed, the vectors defined by Equation 3 can be thought of as world locations, corresponding to the relative position of the walker on the grid, divided by the time left. In fact, these vectors condense the spatial and temporal aspects of the world in a way that is sufficient for prediction. Thus, these world-model-like representations can be putatively traced back to a specific interaction between data, architecture and training: the minimal energy-based formulation of the data’s predictive geometry relies on position vectors, and the network itself processes vectors optimally with respect to a prediction objective. In other words, the world model is already implicit in the predictive structure of the system—the network simply has the right architecture and training objective to capture it. The grid walker thus serves as a proof of concept: a setting where the emergence of world-model representations from predictive geometry can be verified analytically.

4.3 PREDICTIVE GEOMETRY AS GRAMMAR

The step emissions of the grid walkers produce length- T sequences of a regular language (Section 3.1). The formulation of such a formal language, however, is not enough to describe the walker—its stochastic nature provides an additional important ingredient. Indeed, the uniform distribution of valid paths is not information about validity, but occurrence—one may venture here a loose analogy with semantics, where the difference between sentences such as “*I’m feeling blue*” and “*I’m feeling green*” is not about syntactic correctness, but context-dependent usage frequency. Notably, contemporary frontier LLMs must model both deterministic/formal/syntactic rules and stochastic/informal/semantic ones based on a training objective that is solely probabilistic.

In our simple lattice model, a single parameter controls the degree of stochasticity of the next step, *i.e.*, the remaining time $T - t - 1$. It plays an explicit role as the temperature in the Gibbs measure over the next steps, Equation 4. As $t \rightarrow T - 1$, the distribution becomes deterministic¹. Moreover, since the logits attain their maximum when the displacement $\Delta \in \{\Delta_L, \Delta_R, \Delta_D, \Delta_U\}$ is antiparallel to the vector $x_t - p$, the next-step distribution faithfully expresses the formal grammatical rule of the language—arriving at p after T timesteps.

Hence, the sufficiently predictive vectors of Equation 3 learned by the transformer encode, on the one hand, the temperature—and therefore stochasticity—in their length; on the other hand, the angle between these vectors is also crucial to model the formal rule. This geometric structure is thus sufficient to describe both the stochastic and formal aspects of the simple lattice language under consideration. This perspective again appears trivial in this case, but we believe in the possibility that similar geometric structures might underlie more complex languages as well—it might be a matter of understanding how to decompose them into simpler parts.

4.4 BELIEF STATES OF THE GRID WALKER

Whereas the previous work discussed in Section 2.1 focused on ergodic HMMs and their belief states, here we focus on predictive states instead. These two, however, are related. It can be shown that belief states can always be linearly mapped to predictive states, but not the other way around (see Riechers et al. (2025b) and this paper’s Appendix A.4). This means that the dimensionality of the belief-state space is an upper bound to that of the predictive states, even if one takes infinite future horizons into account. Our time-inhomogeneous HMM, however, has a somewhat uninteresting belief-state space: the transitions between states are deterministic given observations (more about this in Section 5). This gives a very loose dimension upper bound, as we know that the intrinsic dimensionality of predictive states is two². Thus, our example shows how exploring the geometric structure of predictive states, rather than belief states, can be more informative in some settings.

¹We ignore the regime assumptions of the approximation in this analysis because it holds on a qualitative level.

²The upper bound of the 4-dimensional next-step predictive state we use is already 3, but the 2-dimensional manifold structure of predictive states holds even for infinite time horizons.

5 LIMITATIONS AND FUTURE CHALLENGES

Two important caveats should be immediately recognized. Firstly, there is the issue of scalability and generalization—our toy system is deliberately simple, which makes this kind of analytical examination possible, whereas in most systems such an analysis does not appear to be feasible. Despite these challenges, it is known that neural networks often find these world-like representations without direct supervision, even in more complex settings (Gurnee and Tegmark (2024); Karvonen (2024); Ivanitskiy et al. (2023)). In order to trace these representations back to the system’s generative or predictive structure, a decomposition method is necessary to break complex structures into tractable ones. There are preliminary findings which suggest that the theory of Markov processes, optimal prediction and computational mechanics might provide the right theoretical framework for this task (Shai et al. (2026)).

Secondly, an important distinction needs to be made between generation and prediction, which are confounded in our specific setting. In general, generation relies on state-dependent computation, but this state might be hidden from an external observer that wishes to make observable predictions. However, since the initial and final states are always the same for each trained network, and since the underlying model has deterministic state transitions given a walk step (L , R , D or U), there is no relevant information about the states that is hidden from the observer (the Transformer in our case). Therefore, an optimal predictive model coincides with the most parsimonious generative model. Studying an example for which states are fundamentally hidden, such as in Shai et al. (2024), might provide new insights.

Moreover, the assumption of using finite HMMs as generative models might be too restrictive if the goal is to apply these frameworks to languages higher in the Chomsky hierarchy, such as context-free grammars (CFGs), let alone natural language itself. Predictive states, unlike belief states, are not restricted to HMMs, so it may be useful to better understand the relationship between these and other objects such as probabilistic CFGs. We postpone a detailed investigation of this significant issue to future work.

Another important aspect that warrants further investigation is the absence of an explicit assessment of generalization. In particular, it would be valuable to examine how representational alignment with predictive vectors relates to, and potentially predicts, the model’s ability to generalize beyond the training distribution.

6 CONCLUSIONS

After training transformer neural networks to predict the movements of constrained 2d-lattice walkers described in Section 3.1, we found that their internal representations resemble world models for these walkers, and they strongly match the 2-dimensional sufficient vectors for prediction, *i.e.*, the position on the grid divided by the time left. This shows a very simple scenario in which the relationship between the world model and the stochastic structure of the system can be traced back analytically. It also supports a hypothesis outlined in Shai et al. (2024), which posits that artificial neural networks trained on next-token prediction internally represent belief states in order to perform Bayesian belief updates in context.

The full sequences of steps that these walkers produce are strings in a simple finite regular language, so this system also serves as an elementary example of how grammatical rules can be encoded by a neural network under the same principle of optimal prediction—an alternative but complementary perspective to that of world models. The network not only encodes the distance to the enforced endpoint on the grid, thus keeping track of syntax, but it also stores information about the remaining time, thereby keeping track of stochastic freedom, which decreases as time runs out and the walker must approach the goal.

These results encourage a deeper investigation into more complex languages, possibly starting with context-free grammars. Ultimately, the goal is to investigate how universal is the alignment between

the geometry of internal representations in predictive neural networks and predictive/belief states, with the hope that we can someday rely on this putative natural alignment for interpretability and steering.

REFERENCES

- A. Ansuini, A. Laio, J. H. Macke, and D. Zoccolan. Intrinsic dimension of data representations in deep neural networks. In H. Wallach, H. Larochelle, A. Beygelzimer, F. d'Alché-Buc, E. Fox, and R. Garnett, editors, *Advances in Neural Information Processing Systems*, volume 32. Curran Associates, Inc., 2019. URL https://proceedings.neurips.cc/paper_files/paper/2019/file/cfccc0621b49c983991ead4c3d4d3b6b-Paper.pdf.
- G. Boleda. Distributional Semantics and Linguistic Theory. *Annual Review of Linguistics*, 6(1): 213–234, 2020. ISSN 2333-9683. doi: 10.1146/annurev-linguistics-011619-030303.
- T. Brown, B. Mann, N. Ryder, M. Subbiah, J. D. Kaplan, P. Dhariwal, A. Neelakantan, P. Shyam, G. Sastry, A. Askell, S. Agarwal, A. Herbert-Voss, G. Krueger, T. Henighan, R. Child, A. Ramesh, D. Ziegler, J. Wu, C. Winter, C. Hesse, M. Chen, E. Sigler, M. Litwin, S. Gray, B. Chess, J. Clark, C. Berner, S. McCandlish, A. Radford, I. Sutskever, and D. Amodei. Language models are few-shot learners. In H. Larochelle, M. Ranzato, R. Hadsell, M. Balcan, and H. Lin, editors, *Advances in Neural Information Processing Systems*, volume 33, pages 1877–1901. Curran Associates, Inc., 2020. URL https://proceedings.neurips.cc/paper_files/paper/2020/file/1457c0d6bfc4967418bfb8ac142f64a-Paper.pdf.
- K. Clark, U. Khandelwal, O. Levy, and C. D. Manning. What does BERT look at? an analysis of BERT’s attention. In T. Linzen, G. Chrupała, Y. Belinkov, and D. Hupkes, editors, *Proceedings of the 2019 ACL Workshop BlackboxNLP: Analyzing and Interpreting Neural Networks for NLP*, pages 276–286, Florence, Italy, Aug. 2019. Association for Computational Linguistics. doi: 10.18653/v1/W19-4828. URL <https://aclanthology.org/W19-4828/>.
- A. Coenen, E. Reif, A. Yuan, B. Kim, A. Pearce, F. Viégas, and M. Wattenberg. Visualizing and Measuring the Geometry of BERT, 2019.
- J. P. Crutchfield and K. Young. Inferring statistical complexity. *Phys. Rev. Lett.*, 63:105–108, Jul 1989. doi: 10.1103/PhysRevLett.63.105. URL <https://link.aps.org/doi/10.1103/PhysRevLett.63.105>.
- P. Diego-Simón, S. D’ Ascoli, E. Chemla, Y. Lakretz, and J.-R. King. A polar coordinate system represents syntax in large language models. In A. Globerson, L. Mackey, D. Belgrave, A. Fan, U. Paquet, J. Tomczak, and C. Zhang, editors, *Advances in Neural Information Processing Systems*, volume 37, pages 105375–105396. Curran Associates, Inc., 2024. doi: 10.52202/079017-3344. URL https://proceedings.neurips.cc/paper_files/paper/2024/file/be36e50757bf9cd280aa74f89a7d1c23-Paper-Conference.pdf.
- J. Ferrando, G. Sarti, A. Bisazza, and M. R. Costa-jussà. A primer on the inner workings of transformer-based language models. *CoRR*, abs/2405.00208, 2024. URL <https://doi.org/10.48550/arXiv.2405.00208>.
- M. Finlayson, A. Mueller, S. Gehrmann, S. Shieber, T. Linzen, and Y. Belinkov. Causal analysis of syntactic agreement mechanisms in neural language models. In C. Zong, F. Xia, W. Li, and R. Navigli, editors, *Proceedings of the 59th Annual Meeting of the Association for Computational Linguistics and the 11th International Joint Conference on Natural Language Processing (Volume 1: Long Papers)*, pages 1828–1843, Online, Aug. 2021. Association for Computational Linguistics. doi: 10.18653/v1/2021.acl-long.144. URL <https://aclanthology.org/2021.acl-long.144/>.

- W. Gurnee and M. Tegmark. Language models represent space and time. In B. Kim, Y. Yue, S. Chaudhuri, K. Fragkiadaki, M. Khan, and Y. Sun, editors, *International Conference on Learning Representations*, volume 2024, pages 2483–2503, 2024. URL https://proceedings.iclr.cc/paper_files/paper/2024/file/0a6059857ae5c82ea9726ee9282a7145-Paper-Conference.pdf.
- D. Ha and J. Schmidhuber. Recurrent world models facilitate policy evolution. In S. Bengio, H. Wallach, H. Larochelle, K. Grauman, N. Cesa-Bianchi, and R. Garnett, editors, *Advances in Neural Information Processing Systems*, volume 31. Curran Associates, Inc., 2018. URL https://proceedings.neurips.cc/paper_files/paper/2018/file/2de5d16682c3c35007e4e92982f1a2ba-Paper.pdf.
- D. Hafner, J. Pasukonis, J. Ba, and T. Lillicrap. Mastering diverse domains through world models. *Nature*, 640(8059):647–653, 2025. ISSN 1476-4687. doi: 10.1038/s41586-025-08744-2.
- N. Hansen, H. Su, and X. Wang. TD-MPC2: Scalable, robust world models for continuous control. In *The Twelfth International Conference on Learning Representations*, 2024. doi: 10.48550/arXiv.2310.16828.
- J. Hewitt and C. D. Manning. A structural probe for finding syntax in word representations. In J. Burstein, C. Doran, and T. Solorio, editors, *Proceedings of the 2019 Conference of the North American Chapter of the Association for Computational Linguistics: Human Language Technologies, Volume 1 (Long and Short Papers)*, pages 4129–4138, Minneapolis, Minnesota, June 2019. Association for Computational Linguistics. doi: 10.18653/v1/N19-1419. URL <https://aclanthology.org/N19-1419/>.
- P. M. Htut, J. Phang, S. Bordia, and S. R. Bowman. Do Attention Heads in BERT track syntactic dependencies?, 2019.
- M. Ivanitskiy, A. F. Spies, T. Räucher, G. Corlouer, C. Mathwin, L. Quirke, C. Rager, R. Shah, D. Valentine, C. D. Behn, K. Inoue, and S. W. Fung. Linearly structured world representations in maze-solving transformers. In *UniReps: the First Workshop on Unifying Representations in Neural Models*, 2023. URL <https://openreview.net/forum?id=pZakRK1QHU>.
- J. Kaplan, S. McCandlish, T. Henighan, T. B. Brown, B. Chess, R. Child, S. Gray, A. Radford, J. Wu, and D. Amodei. Scaling Laws for Neural Language Models, 2020.
- A. Karvonen. Emergent world models and latent variable estimation in chess-playing language models. In *First Conference on Language Modeling*, 2024. URL <https://openreview.net/forum?id=9n2s817XoQ>.
- S. Kornblith, M. Norouzi, H. Lee, and G. Hinton. Similarity of Neural Network representations revisited. In *Proceedings of the 36th International Conference on Machine Learning*, 2019. doi: 10.48550/ARXIV.1905.00414.
- M. A. Lepori, T. Serre, and E. Pavlick. Uncovering Intermediate Variables in Transformers using Circuit Probing. In *First Conference on Language Modeling*, 2024. URL <https://openreview.net/forum?id=gUNeyiLNxr>.
- K. Li, A. K. Hopkins, D. Bau, F. Viégas, H. Pfister, and M. Wattenberg. Emergent world representations: Exploring a sequence model trained on a synthetic task. In *International Conference on Learning Representations*, 2023.
- N. F. Liu, M. Gardner, Y. Belinkov, M. E. Peters, and N. A. Smith. Linguistic knowledge and transferability of contextual representations. In *Proceedings of the 2019 Conference of the North American Chapter of the Association for Computational Linguistics: Human Language Technologies*, 2019. doi: 10.18653/v1/N19-1112.

- M. López-Otal, J. Gracia, J. Bernad, C. Bobed, L. Pitarch-Ballesteros, and E. Anglés-Herrero. Linguistic Interpretability of Transformer-based Language Models: A systematic review, 2025.
- C. D. Manning, K. Clark, J. Hewitt, U. Khandelwal, and O. Levy. Emergent linguistic structure in artificial neural networks trained by self-supervision. *Proceedings of the National Academy of Sciences*, 2020. doi: 10.1073/pnas.1907367117.
- N. Nanda and J. Bloom. Transformerlens. <https://github.com/TransformerLensOrg/TransformerLens>, 2022.
- M. E. Peters, M. Neumann, L. Zettlemoyer, and W.-t. Yih. Dissecting contextual word embeddings: Architecture and representation. In *Proceedings of the 2018 Conference on Empirical Methods in Natural Language Processing*, 2018. doi: 10.18653/v1/D18-1179.
- M. Piotrowski, P. M. Riechers, D. Filan, and A. S. Shai. Constrained belief updates explain geometric structures in transformer representations. In *Forty-second International Conference on Machine Learning*, 2025. doi: 10.48550/ARXIV.2502.01954.
- A. Radford, J. Wu, R. Child, D. Luan, D. Amodei, and I. Sutskever. Language Models are Unsupervised Multitask Learners. *OpenAI Blog*, 1(8):9, 2019.
- P. M. Riechers, H. R. Bigelow, E. A. Alt, and A. Shai. Next-token pretraining implies in-context learning, 2025a.
- P. M. Riechers, T. J. Elliott, and A. S. Shai. Neural networks leverage nominally quantum and post-quantum representations, 2025b.
- A. Rogers, O. Kovaleva, and A. Rumshisky. A primer in bertology: What we know about how BERT works. *Transactions of the Association for Computational Linguistics*, 8:842–866, 2021. ISSN 2307-387X. doi: 10.1162/tacl.a.00349.
- M. Sahlgren. The distributional hypothesis. *Italian Journal of Linguistics*, 20(1):33–53, 2008.
- A. Shai, L. Amdahl-Culleton, C. L. Christensen, H. R. Bigelow, F. E. Rosas, A. B. Boyd, E. A. Alt, K. J. Ray, and P. M. Riechers. Transformers learn factored representations, 2026.
- A. S. Shai, S. E. Marzen, L. Teixeira, A. G. Oldenziel, and P. M. Riechers. Transformers represent belief state geometry in their residual stream. In *The Thirty-eighth Annual Conference on Neural Information Processing Systems*, 2024. doi: 10.48550/ARXIV.2405.15943. URL <https://openreview.net/forum?id=YIB7REL8UC>.
- C. R. Shalizi and J. P. Crutchfield. Computational mechanics: Pattern and prediction, structure and simplicity. *Journal of Statistical Physics*, 104(3):817–879, 2001. ISSN 1572-9613. doi: 10.1023/A:1010388907793.
- I. Sucholutsky, L. Muttenthaler, A. Weller, A. Peng, A. Bobu, B. Kim, B. C. Love, C. J. Cueva, E. Grant, I. Groen, J. Achterberg, J. B. Tenenbaum, K. M. Collins, K. L. Hermann, K. Otkar, K. Greff, M. N. Hebart, N. Cloos, N. Kriegeskorte, N. Jacoby, Q. Zhang, R. Marjeh, R. Geirhos, S. Chen, S. Kornblith, S. Rane, T. Konkle, T. P. O’Connell, T. Unterthiner, A. K. Lampinen, K.-R. Müller, M. Toneva, and T. L. Griffiths. Getting aligned on representational alignment. *Transactions on Machine Learning Research*, 2023. ISSN 2835-8856. URL <https://openreview.net/forum?id=Hiq71Uh4Yn>.
- I. Tenney, D. Das, and E. Pavlick. BERT rediscovers the classical NLP pipeline. In *Proceedings of the 57th Annual Meeting of the Association for Computational Linguistics*, 2019. doi: 10.18653/v1/P19-1452.
- M. Tucker, P. Qian, and R. Levy. What if this modified that? Syntactic interventions with counterfactual embeddings. In *Findings of the Association for Computational Linguistics: ACL-IJCNLP 2021*, 2021. doi: 10.18653/v1/2021.findings-acl.76.

- P. D. Turney and P. Pantel. From Frequency to Meaning: Vector Space Models of Semantics. *Journal of Artificial Intelligence Research*, 37:141–188, 2010. ISSN 1076-9757. doi: 10.1613/jair.2934.
- A. Vaswani, N. Shazeer, N. Parmar, J. Uszkoreit, L. Jones, A. N. Gomez, L. u. Kaiser, and I. Polosukhin. Attention is all you need. In I. Guyon, U. V. Luxburg, S. Bengio, H. Wallach, R. Fergus, S. Vishwanathan, and R. Garnett, editors, *Advances in Neural Information Processing Systems*, volume 30. Curran Associates, Inc., 2017. URL https://proceedings.neurips.cc/paper_files/paper/2017/file/3f5ee243547dee91fbd053c1c4a845aa-Paper.pdf.
- J. Vig and Y. Belinkov. Analyzing the structure of attention in a transformer language model. In *Proceedings of the 2019 ACL Workshop BlackboxNLP: Analyzing and Interpreting Neural Networks for NLP*, 2019. doi: 10.18653/v1/W19-4808.
- E. Voita, D. Talbot, F. Moiseev, R. Sennrich, and I. Titov. Analyzing multi-head self-attention: Specialized heads do the heavy lifting, the rest can be pruned. In *Proceedings of the 57th Annual Meeting of the Association for Computational Linguistics*, 2019. doi: 10.18653/v1/P19-1580.
- Z. Wu, Y. Chen, B. Kao, and Q. Liu. Perturbed masking: Parameter-free probing for analyzing and interpreting BERT. In *Proceedings of the 58th Annual Meeting of the Association for Computational Linguistics*, 2020. doi: 10.18653/v1/2020.acl-main.383.
- S. M. Xie, A. Raghunathan, P. Liang, and T. Ma. An Explanation of In-context Learning as Implicit Bayesian Inference, 2022.

A APPENDIX

A.1 COMPUTATION OF PROBABILITY DISTRIBUTIONS

All probability distributions used for training and validation are computed exactly via a dynamic-programming recursion, without any sampling or approximation.

Marginal distribution of prefixes. We consider walkers for which all complete paths of length T ending at \mathbf{p} are equally likely: $S_T \sim \text{Unif}\{s_T : \mathbf{x}(s_T) = \mathbf{p}\}$. The marginal distribution of a length- t prefix s_t is obtained by summing over all valid completions,

$$\Pr(S_t = s_t \mid \mathbf{p}) = \sum_{s_{t+1 \rightarrow T}} \Pr(S_T = s_t + s_{t+1 \rightarrow T} \mid \mathbf{p}) \mathbf{1}_{\mathbf{x}(s_T) = \mathbf{p}}, \quad (5)$$

where $s_{t_1 \rightarrow t_2}$ denotes a substring from position t_1 to t_2 and $\mathbf{1}$ is the indicator function. Since $\Pr(S_T \mid \mathbf{p})$ is uniform, this simplifies to a ratio of path counts,

$$\Pr(S_t = s_t \mid \mathbf{p}) = \frac{N_{\mathbf{p}}(\mathbf{x}(s_t))}{N_{\mathbf{p}, T}}, \quad (6)$$

where $N_{\mathbf{p}}(\mathbf{x}(s_t))$ counts valid paths with prefix s_t ending at \mathbf{p} , and $N_{\mathbf{p}, T}$ is the total count. Unlike the full-path distribution, this marginal is not uniform.

Green’s function of the 2D lattice walk. Let $G_n(\mathbf{r})$ denote the number of paths of exactly n steps on \mathbb{Z}^2 starting at the origin and ending at displacement $\mathbf{r} = (r_x, r_y)$. It satisfies the four-neighbor convolution recursion over $\mathcal{E} = \{\Delta_L, \Delta_R, \Delta_D, \Delta_U\}$ (Equation 1),

$$G_n(r_x, r_y) = \sum_{\Delta \in \mathcal{E}} G_{n-1}(r_x - \Delta_x, r_y - \Delta_y), \quad (7)$$

with the initial condition $G_0(\mathbf{0}) = 1$ and $G_0(\mathbf{r}) = 0$ for $\mathbf{r} \neq \mathbf{0}$. Since only positions with the same parity as n are reachable in exactly n steps ($G_n(\mathbf{r}) = 0$ whenever $r_x + r_y \not\equiv n \pmod{2}$), the nonzero entries at step n fit in a $(n+1) \times (n+1)$ triangular array.

Rotated coordinate system. The recursion is implemented in a rotated basis $(i, j) = \left(\frac{r_x+r_y+n}{2}, \frac{r_x-r_y+n}{2}\right)$, which maps the four-neighbor update to four corner additions on a square array and enforces the parity constraint as an integrality condition on (i, j) . All arithmetic is performed in log-space for numerical stability.

Completion counts. The number of valid completions of a partial walk ending at position \mathbf{x}_t after t steps, given endpoint \mathbf{p} and total horizon T , equals

$$N_{\mathbf{p}}(\mathbf{x}_t) = G_{T-t}(\mathbf{p} - \mathbf{x}_t).$$

The total number of valid paths is $N_{\mathbf{p},T} = G_T(\mathbf{p})$, and the prefix probability follows from Equation 6.

Next-step probabilities. The conditional next-step probability is obtained exactly as the ratio

$$\Pr(c_{t+1} | s_t; \mathbf{p}) = \frac{G_{T-t-1}(\mathbf{p} - \mathbf{x}_t - \Delta_{c_{t+1}})}{G_{T-t}(\mathbf{p} - \mathbf{x}_t)}, \quad (8)$$

and is well-defined because $G_{T-t}(\mathbf{p} - \mathbf{x}_t) = \sum_{\Delta \in \mathcal{E}} G_{T-t-1}(\mathbf{p} - \mathbf{x}_t - \Delta)$ by the recursion of Equation 7, so the four numerator terms automatically sum to the denominator. In log-space this ratio is a simple subtraction.

Precomputation. The recursion is run once forward from G_0 to G_T , storing every level. For each valid prefix s_t (indexed by its equivalence class (\mathbf{x}_t, t)), Equation 8 gives an exact probability table over the four next symbols. The full joint distribution over length- τ prefixes is then assembled by multiplying consecutive next-step factors, and these tables are stored in memory for use as training batches and as validation targets.

A.2 APPROXIMATING PATH COUNT FOR GRID WALKER

We derive the Gaussian approximation to $G_n(\mathbf{x})$ that underpins the closed-form expressions in the main text.

Fourier representation. At each time step, the walker takes one of the four displacements $\Delta \in \mathcal{E}$. The characteristic function (Fourier transform) of a single uniform step is the *structure function*

$$\lambda(\mathbf{k}) = \sum_{\Delta \in \mathcal{E}} e^{i\mathbf{k} \cdot \Delta} = e^{ik_x} + e^{-ik_x} + e^{ik_y} + e^{-ik_y} = 2 \cos k_x + 2 \cos k_y, \quad (9)$$

where $\mathbf{k} = (k_x, k_y)$ is the wavevector conjugate to the lattice position. Since the n steps of an unconstrained walk are independent and identically distributed, the characteristic function of the total displacement $\mathbf{x}_n = \sum_{t'=1}^n \Delta_{t'}$ is $\lambda(\mathbf{k})^n$ (by the convolution theorem for sums of independent random variables). Inverting the Fourier transform recovers the number of walks ending at (x, y) ,

$$G_n(x, y) = \frac{1}{(2\pi)^2} \int_{-\pi}^{\pi} \int_{-\pi}^{\pi} e^{i(k_x x + k_y y)} (2 \cos k_x + 2 \cos k_y)^n dk_x dk_y, \quad (10)$$

where the integration is over the first Brillouin zone $[-\pi, \pi]^2$ of the square lattice. Note that $\lambda(\mathbf{0}) = 4$, so the Fourier transform evaluated at $\mathbf{k} = \mathbf{0}$ is $\sum_{(x,y)} G_n(x, y) = 4^n$ as expected (the total number of unrestricted n -step walks). This integral representation is the starting point for the saddle-point approximation below.

Saddle-point evaluation. For large n and modest $\|\mathbf{x}\|$, the integral is dominated by a saddle near $\mathbf{k} = \mathbf{0}$. Expanding the log-characteristic function,

$$\ln(2 \cos k_x + 2 \cos k_y) = \ln 4 - \frac{k_x^2 + k_y^2}{4} + O(k_x^4 + k_y^4),$$

and substituting into Equation 10,

$$G_n(x, y) \approx \frac{4^n}{(2\pi)^2} \int_{-\infty}^{\infty} \int_{-\infty}^{\infty} e^{i(k_x x + k_y y)} e^{-n(k_x^2 + k_y^2)/4} dk_x dk_y.$$

Each factor is a standard Gaussian Fourier transform, $\int e^{ik_x x} e^{-nk_x^2/4} dk_x = 2\sqrt{\pi/n} e^{-x^2/n}$, giving

$$G_n(x, y) \approx \frac{4^n}{\pi n} \exp\left(-\frac{x^2 + y^2}{n}\right). \quad (11)$$

Since $N_{\mathbf{p}}(\mathbf{x}_t) = G_{T-t}(\mathbf{p} - \mathbf{x}_t)$ (the walker has $T - t$ steps remaining to reach \mathbf{p} from \mathbf{x}_t), substituting $n \rightarrow T - t$ and $\mathbf{x} \rightarrow \mathbf{p} - \mathbf{x}_t$ yields

$$N_{\mathbf{p}}(\mathbf{x}_t) \approx 4^{T-t} (\pi(T-t))^{-1} \exp(-\|\mathbf{x}_t - \mathbf{p}\|^2 / (T-t)).$$

Derivation of the next-step formula. Using Equation 11 in Equation 8 and writing $\mathbf{r} = \mathbf{x}_t - \mathbf{p}$,

$$\Pr(c_{t+1} | s_t; \mathbf{p}) \propto G_{T-t-1}(\mathbf{r} + \Delta_{c_{t+1}}) \propto e^{-\|\mathbf{r} + \Delta_{c_{t+1}}\|^2 / (T-t-1)}.$$

Expanding the square,

$$-\frac{\|\mathbf{r} + \Delta\|^2}{T-t-1} = -\frac{\|\mathbf{r}\|^2}{T-t-1} + \frac{2(\mathbf{p} - \mathbf{x}_t) \cdot \Delta}{T-t-1} - \frac{1}{T-t-1},$$

the terms $\|\mathbf{r}\|^2$ and 1 are constant with respect to c_{t+1} and cancel under normalization, so

$$\Pr(c_{t+1} | s_t; \mathbf{p}) \approx \frac{e^{-2 \frac{\mathbf{x}_t - \mathbf{p}}{T-t-1} \cdot \Delta_{c_{t+1}}}}{\sum_{\Delta' \in \mathcal{E}} e^{-2 \frac{\mathbf{x}_t - \mathbf{p}}{T-t-1} \cdot \Delta'}},$$

which is Equation (6) of the main text. The approximation is valid whenever $\|\mathbf{x}_t - \mathbf{p}\| \ll T - t - 1$ (diffusive regime).

General (non-diffusive) saddle-point. The preceding Gaussian approximation is valid only in the diffusive regime $\|\mathbf{x}_t - \mathbf{p}\| \ll T - t - 1$. When the walker's displacement from the endpoint is comparable to the remaining horizon, the quadratic expansion of $\ln \lambda(\mathbf{k})$ around $\mathbf{k} = \mathbf{0}$ is no longer adequate, and one must retain the full structure function $\lambda(\mathbf{k}) = 2 \cos k_x + 2 \cos k_y$ from Equation 9.

Return to the exact Fourier integral of Equation 10 with $n = T - t - 1$ and displacement $\mathbf{r}_t = \mathbf{p} - \mathbf{x}_t - \Delta_{c_{t+1}}$:

$$G_{T-t-1}(\mathbf{r}_t) = \frac{1}{(2\pi)^2} \int_{[-\pi, \pi]^2} e^{-i\mathbf{k} \cdot \mathbf{r}_t} \lambda(\mathbf{k})^{T-t-1} d^2\mathbf{k}.$$

For large $T - t - 1$, the integrand is sharply peaked and the integral can be evaluated by the method of steepest descents (saddle-point approximation). The exponent to be extremized is

$$\Phi(\mathbf{k}) := -i\mathbf{k} \cdot \mathbf{r}_t + (T - t - 1) \ln \lambda(\mathbf{k}).$$

Setting $\nabla_{\mathbf{k}} \Phi = \mathbf{0}$ yields the saddle-point condition

$$\frac{\mathbf{r}_t}{T-t-1} = i \frac{\nabla_{\mathbf{k}} \lambda(\mathbf{k})}{\lambda(\mathbf{k})} \Big|_{\mathbf{k}=\mathbf{k}^*}.$$

Since $\nabla_{\mathbf{k}} \lambda = (-2 \sin k_x, -2 \sin k_y)$, the right-hand side is purely imaginary when \mathbf{k} is real, whereas the left-hand side is real. The saddle therefore lies on the imaginary axis: we set $\mathbf{k}^* = i\mathbf{q}$ with $\mathbf{q} \in \mathbb{R}^2$. Substituting $\cos(iq_c) = \cosh q_c$ and $\sin(iq_c) = i \sinh q_c$, the saddle-point equation becomes the transcendental system

$$u_c = \frac{\sinh q_c}{\cosh q_x + \cosh q_y}, \quad c \in \{x, y\}, \quad \mathbf{u}_t := \frac{\mathbf{x}_t - \mathbf{p}}{T-t-1}, \quad (12)$$

where we used $\mathbf{r}_t = \mathbf{p} - \mathbf{x}_t$ so that $-\mathbf{r}_t/(T-t-1) = \mathbf{u}_t$. Note that the sign of \mathbf{u}_t points from the endpoint towards the current position, encoding how far the walker still needs to travel relative to the time available.

At the saddle, the leading-order evaluation of G_{T-t-1} gives a pre-exponential factor (from the Hessian determinant) times $\exp[\mathbf{q} \cdot \mathbf{r}_t + (T-t-1) \ln \lambda(i\mathbf{q})]$. When forming the next-step probability ratio $G_{T-t-1}(\mathbf{p} - \mathbf{x}_t - \Delta_{c_{t+1}})/G_{T-t}(\mathbf{p} - \mathbf{x}_t)$, the pre-exponential factors and all terms independent of c_{t+1} cancel under normalization. The surviving dependence on the step direction comes from the shift $\mathbf{r}_t \rightarrow \mathbf{r}_t - \Delta_{c_{t+1}}$, which contributes a factor $e^{-\mathbf{q} \cdot \Delta_{c_{t+1}}}$. Identifying $\mathbf{v}_t \equiv \mathbf{q}(\mathbf{u}_t)$, we obtain

$$\Pr(c_{t+1} \mid s_t; \mathbf{p}) \approx \frac{e^{-\mathbf{v}_t \cdot \Delta_{c_{t+1}}}}{\sum_{\Delta' \in \mathcal{E}} e^{-\mathbf{v}_t \cdot \Delta'}},$$

which is the Softmax formula of Equation (5) in the main text, now valid beyond the diffusive regime. The nonlinear map \mathbf{q} defined by the implicit relation of Equation 12 is the one introduced in Section 3.1, so $\mathbf{v}_t = \mathbf{q}((\mathbf{x}_t - \mathbf{p})/(T-t-1))$. In practice, \mathbf{q} is evaluated by numerically inverting Equation 12 for each value of \mathbf{u}_t .

Finally, one can verify that the diffusive limit is correctly recovered. When $\|\mathbf{u}_t\| \ll 1$, we have $\|\mathbf{q}\| \ll 1$ as well, so the hyperbolic functions can be linearized: $\sinh q_c \approx q_c$ and $\cosh q_c \approx 1 + q_c^2/2 \approx 1$. Equation 12 then reduces to $u_c \approx q_c/(1+1) = q_c/2$, giving $\mathbf{q} \approx 2\mathbf{u}_t$ and thus $\mathbf{v}_t \approx 2(\mathbf{x}_t - \mathbf{p})/(T-t-1)$, which recovers the linear formula of Equation (6).

A.3 COMPUTING SUFFICIENT VECTOR

Formal definition. The sufficient vector $\mathbf{v}_t \in \mathbb{R}^2$ is defined implicitly by the requirement that the Softmax formula

$$\Pr(c \mid s_t; \mathbf{p}) = \frac{e^{-\mathbf{v}_t \cdot \Delta_c}}{\sum_{\Delta' \in \mathcal{E}} e^{-\mathbf{v}_t \cdot \Delta'}} \quad (13)$$

holds for all four symbols $c \in \{L, R, D, U\}$. Exactly this relation is guaranteed by the saddle-point analysis described in Appendix A.2, with $\mathbf{v}_t = \mathbf{q}((\mathbf{x}_t - \mathbf{p})/(T-t-1))$.

Inversion from log-probabilities. Taking logarithms of Equation 13 gives

$$\log \Pr(c \mid s_t; \mathbf{p}) = -\mathbf{v}_t \cdot \Delta_c - \log Z(\mathbf{v}_t),$$

so the vector of log-probabilities $\boldsymbol{\ell} \in \mathbb{R}^4$ with entries $\ell_c = \log \Pr(c \mid s_t; \mathbf{p})$ satisfies $\boldsymbol{\ell} = -D\mathbf{v}_t + \lambda \mathbf{1}$ for some scalar λ , where $D \in \mathbb{R}^{4 \times 2}$ is the matrix whose rows are the displacement vectors $\Delta_L, \Delta_R, \Delta_D, \Delta_U$, and $\mathbf{1}$ is the all-ones vector.

The columns of D are orthogonal and satisfy $D^\top D = 2I_2$, so the minimum-norm least-squares solution is

$$\mathbf{v}_t = -\frac{1}{2}D^\top \boldsymbol{\ell} = \frac{1}{2} \begin{pmatrix} \log p_L - \log p_R \\ \log p_D - \log p_U \end{pmatrix}, \quad (14)$$

where $p_c = \Pr(c \mid s_t; \mathbf{p})$. The additive constant λ drops out because $D^\top \mathbf{1} = \mathbf{0}$ (the rows of D sum to zero), so Equation 14 is independent of the gauge choice for the log-probabilities.

Four-dimensional representation. In the representational-alignment analysis of Section 3.4, we use the mean-centered log-probability vector $\bar{\boldsymbol{\ell}} = \boldsymbol{\ell} - \bar{\ell} \mathbf{1}$ (where $\bar{\ell}$ is the mean of the four entries) as the regression target. This four-dimensional vector encodes exactly the same information as \mathbf{v}_t , since $\bar{\boldsymbol{\ell}} = -D\mathbf{v}_t$ (using $D^\top \mathbf{1} = \mathbf{0}$), and the two representations are interconvertible via Equation 14 and its inverse. The centered representation is convenient for the regression because it removes the uninformative overall scale.

Numerical computation. In practice, the exact log-probabilities ℓ are obtained from the Green’s function via Equation 8: for each equivalence class (\mathbf{x}_t, t) , we compute $G_{T-t-1}(\mathbf{p} - \mathbf{x}_t - \Delta_c)$ for all four Δ_c in log-space, normalize by their log-sum-exp, and store the result as the target for training and evaluation. The 2D form of Equation 14 is used for visualization and interpretability, while the 4D form is used for regression.

Analyticity of \mathbf{q} . The map \mathbf{q} is the inverse of $F : \mathbb{R}^2 \rightarrow \mathcal{D}$, where $\mathcal{D} = \{\mathbf{u} : |u_x| + |u_y| < 1\}$ is the physically admissible domain (a lattice walk cannot displace faster than one unit per step on average, so $|u_x| + |u_y| < 1$ always holds), and F is defined componentwise by Equation 12: $F_c(\mathbf{q}) = \sinh q_c / (\cosh q_x + \cosh q_y)$. Since F is a ratio of hyperbolic functions it is real-analytic on \mathbb{R}^2 . Its 2×2 Jacobian has entries

$$\frac{\partial F_x}{\partial q_x} = \frac{1 + \cosh q_x \cosh q_y}{(\cosh q_x + \cosh q_y)^2}, \quad \frac{\partial F_x}{\partial q_y} = \frac{-\sinh q_x \sinh q_y}{(\cosh q_x + \cosh q_y)^2},$$

and analogously with $x \leftrightarrow y$ for ∂F_y . A short computation gives

$$\det J_F(\mathbf{q}) = \frac{1}{(\cosh q_x + \cosh q_y)^2} > 0 \quad \forall \mathbf{q} \in \mathbb{R}^2.$$

Since J_F is nowhere singular and F is real-analytic, the analytic inverse function theorem guarantees that $\mathbf{q} = F^{-1} : \mathcal{D} \rightarrow \mathbb{R}^2$ is also real-analytic—and in particular C^∞ —on its entire domain.

A.4 MAPPING BETWEEN BELIEF AND PREDICTIVE STATES

Here we make precise the distinction between *belief states* and *predictive states* for the grid walker, and explain why the latter offer a more informative low-dimensional characterization.

Belief states. For a general hidden-Markov model (HMM), the belief state at time t given observation history s_t is the posterior distribution over hidden states, $\mu_t = \Pr(X_t = \cdot \mid s_t)$. In our grid walker, the hidden state at time t is the position $X_t = \mathbf{x}_t \in \mathbb{Z}^2$. Since each step deterministically updates the position ($\mathbf{x}_t = \sum_{t'=1}^t \Delta_{c_{t'}}$ is fully determined by the observation sequence), the belief state is

$$\mu_t(\mathbf{x}) = \Pr(X_t = \mathbf{x} \mid s_t) = \delta_{\mathbf{x}, \mathbf{x}(s_t)},$$

a point mass concentrated at the current position $\mathbf{x}(s_t)$. The belief-state space at depth t therefore consists of all positions reachable in t steps, a set of size $O(t^2)$ that grows without bound with t .

Predictive states. The predictive state at time t , by contrast, is the distribution over future observations:

$$\psi_t = \Pr(S_{t+1:T} = \cdot \mid s_t; \mathbf{p}).$$

Two histories s_t and s'_t are *causally equivalent* if $\psi_t = \psi'_t$, *i.e.*, if they produce identical predictive distributions for all futures. From Equation 8, the predictive distribution depends on s_t only through the pair $(\mathbf{x}(s_t), t)$: all histories that share the same position at the same time step are causally equivalent. The space of predictive states is therefore parameterized by (\mathbf{x}_t, t) , and via the continuous sufficient vector $\mathbf{v}_t = \mathbf{q}((\mathbf{x}_t - \mathbf{p}) / (T - t - 1))$, it is embedded in a two-dimensional manifold inside Δ^3 (the 3-simplex of probability vectors over four symbols).

Linear map from belief states to predictive states. For any HMM, there exists a linear map Φ such that $\psi_t = \Phi \mu_t$. This map is constructed as follows. Let \mathcal{X} be the set of possible positions at time t ; then

$$\Pr(c \mid s_t; \mathbf{p}) = \sum_{\mathbf{x} \in \mathcal{X}} \mu_t(\mathbf{x}) \Pr(c \mid X_t = \mathbf{x}; \mathbf{p}) = \Pr(c \mid X_t = \mathbf{x}(s_t); \mathbf{p}),$$

where the last equality holds because μ_t is a point mass. In general, even when μ_t is spread over several states, the map $\mu_t \mapsto \Pr(\cdot \mid s_t; \mathbf{p})$ is linear in the belief state. The inverse map does not exist

in general: multiple belief states may yield the same predictive state, and in our setting the converse is trivially true—the single nonzero component of μ_t amounts to consulting one row of the matrix $[\Pr(c \mid X_t = \mathbf{x}; \mathbf{p})]_{\mathbf{x},c}$.

Dimension comparison. The belief-state space at depth t is $(|\mathcal{X}_t| - 1)$ -dimensional (a simplex over the reachable positions), with $|\mathcal{X}_t| = O(t^2)$. The predictive-state space is two-dimensional, as argued in Appendix A.5. The inequality $\dim(\mathcal{P}) \leq \dim(\mathcal{B})$ predicted by the general theory holds, but in a degenerate way: the bound is so loose (2 vs. $O(t^2)$) that it is largely uninformative here. Working directly with predictive states rather than belief states therefore yields a far more compact and geometrically meaningful characterization of the walker’s computational structure—even though the belief-state update is trivial (a deterministic point-mass shift), the predictive-state geometry captures the relevant stochastic and spatial structure of the process.

A.5 DIMENSIONALITY OF THE PREDICTION MANIFOLD

Fix t and consider the next-step map $f : \mathbb{R}^2 \rightarrow \Delta^3$ defined by $f(\mathbf{x}_t) := \Pr(\cdot \mid s_t)$, where we analytically extend the closed-form expressions to continuous \mathbf{x}_t . Whenever f is differentiable, the rank theorem implies that the image of f is locally contained in a submanifold of dimension at most $\text{rank}(Df) \leq 2$, with possible lower-dimensional degeneracies at points where $\text{rank}(Df) < 2$.

In statistical mechanics, the Softmax distribution is referred to as the Boltzmann distribution. In the present setting, the “microstates” are the four possible next-step symbols $c_{t+1} \in \{L, R, D, U\}$ (equivalently, their displacements $\Delta_{t+1} \in \mathcal{E}$), and their corresponding “energies” can be identified (up to an additive constant and overall scale) with a quantity linear in the current position \mathbf{x}_t ; concretely, Equation 4 implies

$$\Pr(c_{t+1} \mid s_t; \mathbf{p}) \propto \exp(-\beta_t \epsilon(c_{t+1}; s_t, \mathbf{p})),$$

$$\beta_t := \frac{1}{T - t - 1}, \quad \epsilon(c_{t+1}; s_t, \mathbf{p}) := 2(\mathbf{x}_t - \mathbf{p}) \cdot \Delta_{t+1},$$

so that decreasing “energy” corresponds to choosing a step whose displacement points towards the endpoint (i.e., towards reducing $\|\mathbf{x}_t - \mathbf{p}\|$). The prefactor β_t plays the role of an inverse temperature that increases as $t \rightarrow T - 1$, reflecting the fact that randomness must decrease as the path approaches its fixed horizon; correspondingly, the approximation becomes singular at $t = T - 1$, where one may replace the Softmax by a hard maximization. Finally, since the logits are given by $D\mathbf{x}_t$ up to scaling, the effective logit (and thus probability) vectors necessarily lie in a two-dimensional subspace determined by the rank of D , and the position \mathbf{x}_t acts as a sufficient statistic for predicting future steps (including multi-step predictive distributions) given the endpoint.

A.6 HYPERPARAMETERS

All hyperparameters were directly taken from Riechers et al. (2025b). All models are instances of the `HookedTransformer` architecture from the `TransformerLens` library (Nanda and Bloom, 2022), a decoder-only transformer with $L = 4$ layers, $H = 4$ attention heads, head dimension $d_{\text{head}} = 32$ (model dimension $d_{\text{model}} = 128$), MLP width $d_{\text{mlp}} = 512$ with ReLU activations, and LayerNorm normalization. The context window is fixed to $\tau = 8$ tokens. Training ran for 20 000 epochs of 200 minibatches of size 256. Networks were trained with PyTorch’s Adam optimizer with default betas, eps and weight_decay parameters—(0.9, 0.999), 10^{-8} and 0, respectively—and an initial learning rate of $5 \cdot 10^{-5}$. This learning rate was adjusted by PyTorch’s scheduler `optim.lr.scheduler.ReduceLRonPlateau`, with parameters `factor=0.5`, `patience=1000`, `cooldown=200`, `threshold=1e-6`.